Article

Aerodynamic roughness of rippled beds under active saltation at Earth-to-Mars atmospheric pressures

Carlos A. Alvarez [1] ✉, **Mathieu G. A. Lapôtre** [1], **Christy Swann** [2], **Ryan C. Ewing**[3], **Pan Jia**[4] & **Philippe Claudin**[5]

As winds blow over sand, grains are mobilized and reorganized into bedforms such as ripples and dunes. In turn, sand transport and bedforms affect the winds themselves. These complex interactions between winds and sediment render modeling of windswept landscapes challenging. A critical parameter in such models is the aerodynamic roughness length, z_0, defined as the height above the bed at which wind velocity predicted from the log law drops to zero. In aeolian environments, z_0 can variably be controlled by the laminar viscous sublayer, grain roughness, form drag from bedforms, or the saltation layer. Estimates of z_0 are used on Mars, notably, to predict wind speeds, sand fluxes, and global circulation patterns; yet, no robust measurements of z_0 have been performed over rippled sand on Mars to date. Here, we measure z_0 over equilibrated rippled sand beds with active saltation under atmospheric pressures intermediate between those of Earth and Mars. Extrapolated to Mars, our results suggest that z_0 over rippled beds and under active saltation may be dominated by form drag across a plausible range of wind velocities, reaching values up to 1 cm—two orders of magnitude larger than typically assumed for flat beds under similar sediment transport conditions.

Interactions between winds and sediment occur over a wide range of scales, from the mobilization of individual sand grains to the formation of bedforms and overall landscape evolution. Such interactions are governed by the shear stress imparted by winds onto the sediment bed; in turn, the bed's response to shearing winds affects the wind profile, and thus, bed stresses[1]. Determining basal wind stresses is thus critical to predicting sand fluxes and landscape evolution in response to winds across planetary bodies.

The shear stress imparted by winds onto a surface, τ_b, is controlled by a length scale, known as the aerodynamic roughness length, z_0. This length scale is the height at which wind speed is predicted to become null under neutral atmospheric conditions—that is, when temperature-driven buoyancy effects are negligible-such that

$$u(z) = \frac{u_*}{\kappa} ln\left(\frac{z}{z_0}\right), \qquad (1)$$

where $u(z)$ is the vertical wind velocity, $u_* = \sqrt{\tau_b/\rho}$ is the shear velocity (with ρ the atmospheric density), and $\kappa \approx 0.41$ is the von Kármán constant. The parameter z_0 can also be interpreted as a mixing length governing turbulent fluctuations over a solid surface[2]. It plays an essential role in boundary layer dynamics and controls energy exchanges between planetary surfaces and overlying atmospheres[3]. For example, characterizations of z_0 are required to understand how

[1]Department of Earth & Planetary Sciences, Stanford University, Stanford, CA, USA. [2]RCOAST, New Orleans, LA, USA. [3]Astromaterials & Exploration Science Division, NASA Johnson Space Center, Houston, TX, USA. [4]School of Science, Harbin Institute of Technology, Shenzhen, PR China. [5]Physique et Mécanique des Milieux Hétérogènes, UMR 7636 CNRS—ESPCI Paris—Université PSL—Université Paris Cité—Sorbonne Université, Paris, France. ✉ e-mail: calvare7@stanford.edu

topography, vegetation, and other obstacles impact wind patterns on Earth[4–8]. It also plays a crucial role in regulating the vertical exchange of heat between the surface and the atmosphere[9,10].

The value of z_0 varies with the characteristics of planetary surfaces. Over sand beds with a typical length scale, r, of bed roughness elements (such as individual grains or bedforms), one can define a roughness-based Reynolds number,

$$\mathrm{Re}_r = \frac{r u_*}{\nu}, \qquad (2)$$

where ν is the kinematic viscosity of the atmosphere[11]. When $\mathrm{Re}_r \lesssim 10$, the bed is said to be aerodynamically smooth. In the absence of saltation, z_0 for aerodynamically smooth beds is controlled by the thickness of the laminar sublayer[12], such that

$$z_0 = \frac{\nu}{9 u_*}. \qquad (3)$$

In turn, when $\mathrm{Re}_r \gtrsim 100$ and sand is immobile, the bed is said to be aerodynamically rough, and z_0 is controlled by r. For flat beds (i.e., in the absence of bedforms), r scales with grain size. Ref. 13 determined experimentally that z_0 is given by $k_s/30$, where k_s is the equivalent sand-grain roughness height. For mixed grain populations, $k_s \approx n d_i$, where n is of the order 2–3, and d_i is the i th percentile of the grain size distribution (often d_{50}, d_{65}, or d_{95})[14–16]. Thus,

$$z_0 \approx \frac{d_{50}}{12}. \qquad (4)$$

As grains are lifted from the surface by winds and saltate (following a series of short, ballistic trajectories before impacting the surface again), a saltation layer forms, which reduces the wind speed near the surface, steepening the velocity profile[17,18]. This feedback between saltation and the wind profile prevents the saltation layer from growing unchecked at an exponential rate to any height above the surface[19]. In this case, z_0 is influenced by the thickness of the saltation layer.

Under terrestrial conditions, the thickness of the saltation layer was shown to relate to the so-called focal point, defined as the vertical height above which saltation does not affect the wind profile[17]. Below the focal height, H_f, the average upward grain velocity is independent of wind shear velocity, u_*. At the focal point, the wind velocity, U_f, scales with the threshold shear velocity, u_{*t}. Considering the continuity of the velocity profile at the focal point, the aerodynamic roughness length imparted by active saltation can be expressed as

$$z_0 = H_f \, \exp\left(-\kappa \frac{U_f}{u_*}\right). \qquad (5)$$

However, there is no consensus on how parameters such as grain size affect H_f and U_f. For example, it is unclear whether H_f scales linearly with d[20,21], with $\sqrt{d}$[22,23], or not at all[21]. If one of the latter two models is correct, then dimensional analysis dictates that another parameter, likely the kinematic viscosity of air, ν, also controls the position (and possibly the very existence) of the focal point[21–23]; Methods). In the following, we test two different formulations for H_f[21,22], which both account, at least partially, for variations in atmospheric density through kinematic viscosity (Methods).

Whereas no accepted analytical expression exists to date for the focal height and velocity, it was shown experimentally that in the presence of active saltation, the aerodynamic roughness follows an empirical relationship of the form

$$z_0 = \frac{C u_*^2}{2 g}, \qquad (6)$$

where C is a constant that varies with the type of surface or environment[18,24,25]. In this study, we assume $C = 0.01$[26].

Through saltation, the bed often self-organizes into bedforms, such as ripples or dunes. These bedforms disturb the flow, increasing form drag. In aeolian systems featuring multiple bedform scales, both skin friction from grain roughness and form drag from all scales of bedforms affect z_0. To estimate z_0 in such complex conditions, ref. 2 developed a semi-analytical model (here referred to as Jia et al., 2023; Methods) for multiscale roughness, which includes skin friction and form drag from two scales of bedforms through looped calculations (Methods). However, this model does not capture the effect of active saltation over a rippled bed.

On Earth, wind flows are typically aerodynamically rough, and z_0 is controlled by either the surface roughness (below the transport threshold, u_{*t}) or the thickness of the transport layer (above it)[27]. In turn, surface roughness compounds both skin friction (Eq. (4)) and form drag ([2]). Whereas models for z_0 are relatively well established for Earth (Eqs. (3)–(6)), several factors complicate the application of Earth-based models to Mars, severely impeding predictive capabilities for a broad range of phenomena, from dust lifting[28–30] to sand fluxes[31,32] and aeolian erosion rates[33–35].

First, as atmospheric density decreases, atmospheric kinematic viscosity increases, thickening the viscous sublayer. As a result, the roughness-based Reynolds number decreases (for a given roughness scale and shear velocity; Eq. (2)), increasing the likelihood of aerodynamically smooth wind events, and thus, of z_0 being influenced by the laminar sublayer (Eq. (3)). However, it is unclear whether this effect is annulled by active saltation under Mars-like conditions (Eqs. (5)–(6)).

Second, under low-pressure conditions, two types of windblown ripples may emerge—impact ripples and drag ripples[11,20,36–40]. Aeolian drag ripples are analogous to subaqueous ripples[41,42] and aeolian dunes[11,20,38], and result from a hydrodynamic instability that only arises under aerodynamically smooth conditions[11,20,39,40]. On Mars, aeolian drag ripples are characterized by meter-scale wavelengths and decimeter-scale heights, possibly enhancing the role of form drag relative to the case of Earth's much more subdued impact ripples[43].

Measurements of z_0 have been performed over coarse regolith and rocky surfaces on Mars before[44], but never over active sandy rippled beds, such that it remains unknown whether the thicker boundary layer and multiple ripple scales impact z_0 under active transport conditions. Here, we measure the aerodynamic roughness of rippled sand beds under varying atmospheric pressures. For the first time, we characterize the behavior of z_0 in low-pressure wind tunnel experiments in which two scales of ripples (impact and drag ripples) form and active saltation is present.

Results and discussion

Aerodynamic roughness of rippled beds under active saltation

Experiments were conducted over beds of loose sand-sized proxy material (~195 μm crushed nutshells) at freestream wind velocities exceeding the corresponding freestream threshold for the onset of saltation by about 20%. Beds were allowed to develop bedforms and equilibrate (Figs. 1c and 2)[40] before vertical wind profiles were measured using a variable-height pitot tube at a frequency of 0.3 Hz (Fig. 1d). Measurements were performed at 4–5 different heights above the bed, and averaged over 45–60 s at each height[40] (Methods). Wind profiles were measured at 1020, 500, 100, and 50 mbar, and z_0 was derived from those measurements by finding the best fit (u_*, z_0) values using the logarithmic law (Eq. (1); Figs. 3 and 4; Methods). These experiments, which capture the correct physical regimes despite
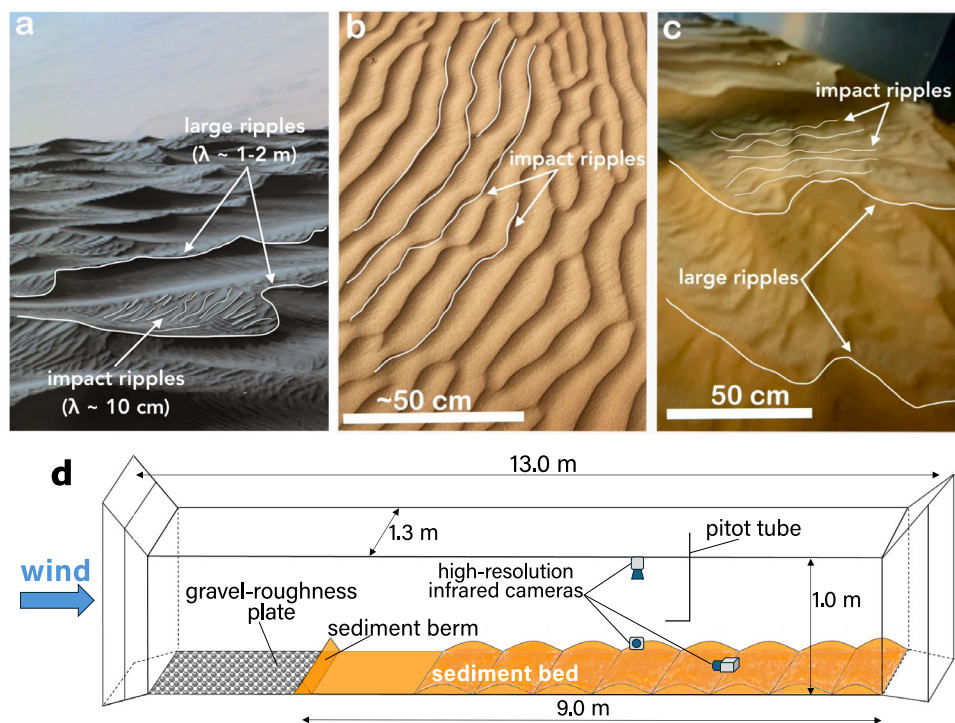
Fig. 1 | Windblown ripples under varied pressure conditions and experimental setup. a Impact ripples superimposed on large wind ripples atop Namib dune, Gale Crater, Mars (Curiosity rover Mastcam mosaic mcam005410, sol 1192; credit: NASA/JPL-Caltech/MSSS). **b** Impact ripples in Al Wusta, Oman. **c** Two scales of windblown ripples at equilibrium, formed in the Mars Surface Wind Tunnel (MARSWIT) at the NASA Ames Research Center under 50 mbar. **d** Schematic representation of the Mars Surface Wind Tunnel (MARSWIT) experimental setup.
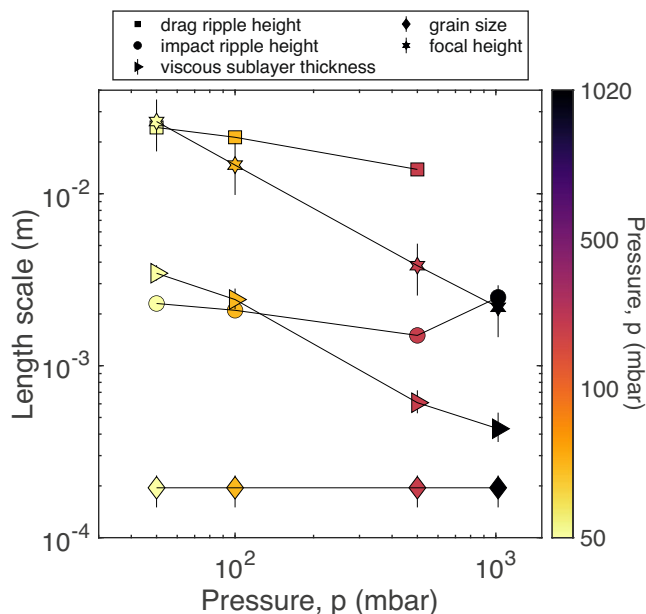
Fig. 2 | Evolution of relevant length scales with atmospheric pressure during wind-tunnel experiments. The presented scales include the grain size (reported as d_{50} with error bars encompassing d_{16}–d_{84}), the thickness of the laminar sublayer (calculated in the absence of saltation), impact (h_i) and drag-ripple (h_l) heights, and height of the focal point, (H_f, Eq. (9)). The latter relates to the thickness of the transport layer and is calculated as described in Methods. Error bars are reported but smaller than most symbols. Source data are provided as a Source Data file.

higher absolute pressures than on Mars, allow us to extrapolate observations to Mars-like surface conditions (Supplementary Text S1 and Supplementary Table S1).

Decimeter-scale impact ripples formed at all pressures[45], whereas larger, drag ripples only formed at pressures less than terrestrial (Fig. 2), as predicted by drag-ripple theory[11,20,40]. The size of drag ripples increased with decreasing atmospheric pressure, consistent with observations on Mars[36,38,46] (Fig. 1a). Similarly, the thickness of the viscous sublayer in the absence of saltation (calculated as $11.6 \frac{\nu}{u_*}$) is expected to increase by about one order of magnitude from ambient terrestrial pressure to 50 mbar (Fig. 2).

Like several of the relevant length scales (Fig. 2), measured z_0 values increase with decreasing atmospheric pressure, from $\approx 2 \times 10^{-4}$ m at 1020 mbar to over 5×10^{-4} m at 50 mbar under our experimental conditions (Fig. 4a). Similarly, predicted values of z_0 from viscous sublayer thickness and saltation increase with decreasing pressure (Fig. 4b) due to decreasing atmospheric density and increasing threshold of motion, respectively (Supplementary Fig. S3).

Derived values of z_0 are compared against model predictions (Fig. 4b; Eqs. (3)–(6); and model of ref. 2; Methods). The large discrepancy between measured z_0 and that expected from the viscous sublayer model is consistent with either aerodynamically rough conditions (at 1020 mbar) or disruption of the viscous sublayer by saltation at all pressures. At 1020 mbar, the model of ref. 2, which predicts the compounded effect of skin friction and form drag from impact ripples, is dominated by skin friction and underpredicts the measured z_0 value, confirming that saltation (Eq. (6)) is the dominant control on z_0 under Earth-like conditions. At all pressures, observed z_0 are most closely matched by the empirical saltation model (Eq. (6)) and the compound form drag model of ref. 2. However, both models consistently underpredict z_0, suggesting that both saltation and form drag contribute to overall aerodynamic roughness.

Next, we investigate the relative influence of saltation and form drag on z_0. To estimate the contribution of saltation to z_0 based on our experimental measurements, we use the model of ref. 2 in an inverse fashion (Methods). Specifically, we adjust the value of an effective
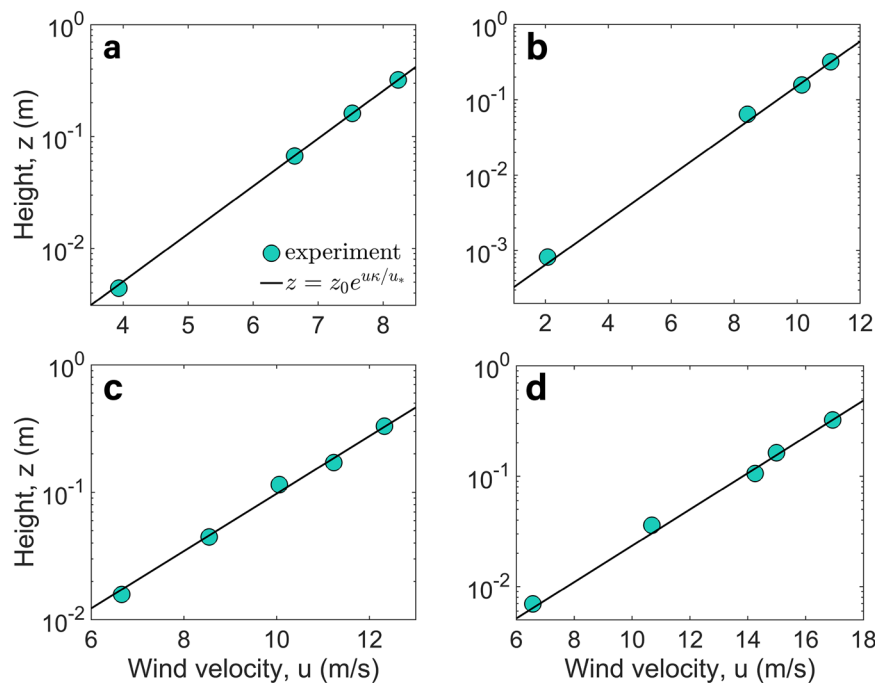
Fig. 3 | Measured vertical wind velocity profiles at varying pressures with corresponding fits to the logarithmic law (Eq. (1)). Profiles are shown for atmospheric pressures of **a** 1020 mbar, **b** 500 mbar, **c** 100 mbar, and **d** 50 mbar.

grain size in this model such that, given the observed bedform dimensions at each pressure, it produces the correct, observed value of z_0. Assuming that skin friction is negligible relative to other roughness contributors under active saltation (Fig. 4b), the effective grain size parameter, instead of grain size, represents a characteristic length scale associated with the saltation layer, from which $z_{0,\text{saltation}}$ can be calculated (Fig. 5; Methods;[2]).

The relative influence of saltation on total aerodynamic roughness, $z_{0,\text{saltation}}/z_0$, varies in a nonlinear fashion with atmospheric pressure (Fig. 5a). Specifically, we find that $z_{0,\text{saltation}}$ is about 80% of z_0 at 1020 mbar, when only subdued impact ripples are present. As pressure decreases and drag ripples form, the contribution of saltation to z_0 drops to 45% at 500 mbar, and increases again progressively under our experimental conditions as pressure decreases, to reach about $\approx$90% at 50 mbar (Fig. 5b).

Focal point at low pressure
Although the existence of a focal point is well established under terrestrial conditions (e.g.,[47–51]), how viscosity may influence its existence, and if it exists, its behavior at low atmospheric pressures remain unknown. Here, we test its existence and behavior by (i) inverting for H_f and U_f from $z_{0,\text{saltation}}$ using Eq. (5) and (ii) comparing H_f and U_f values with the models of refs. 22,[21].

Based on dimensional analysis, theory, and empirical observations, refs. 22,[21] proposed formulations for focal height and velocity that incorporate the influence of atmospheric density and viscosity (Methods). Each model contains two constant coefficients, α and β (Methods). For both models, best-fit values of α and β were inverted at all pressure conditions by minimizing the difference between the estimated $z_{0,\text{saltation}}$ and those modeled using the formulations of refs. 22,21 (Methods).

Using the model of ref. 22, we find that (i) inverted values of α and β are roughly constant across the investigated pressure range, and (ii) inverted β values closely match that estimated by ref. 22 at Earth pressure (Supplementary Fig. S7). Inverted values of α are of the same order of magnitude as, but differ subtly from, those of ref. 22 at Earth pressure (Supplementary Fig. S7). This small difference is attributed to

the presence of impact ripples in the experiments of ref. 52 (and the form drag they imparted on winds), whereas any contributions from form drag is removed from measured z_0 values here (i.e., α and β are estimated from $z_{0,\text{saltation}}$). These findings suggest that a focal point does exist under all investigated pressures, and that the formulation of ref. 22 appropriately describes the dependency of H_f and U_f on atmospheric density and viscosity.

Whereas sets of α and β values that yield equally good fits to the data could be retrieved from both models, we find that β cannot be reasonably assumed to be constant over the range of investigated pressures under the model of ref. 21, and that $\beta \propto \rho^{-\frac{1}{3}}$ instead (Supplementary Text S2). Thus, the model of ref. 22 appears to capture the dependency of H_f on ρ more adequately, and we adopt that formulation for extrapolations to Mars pressure.

Relative influence of saltation and form drag on aerodynamic roughness
Following the model of ref. 22, $H_f \propto \rho^{-\frac{5}{6}}$ (Eqs. (8)–(9); Methods). Furthermore, the wavelength of drag ripples is proportional to $\rho^{-\frac{2}{3}}$[36–38,40–42]. Thus, under low atmospheric pressures (such that $\text{Re}_r \lesssim 10$), $h_{\max} \propto \rho^{-\frac{2}{3}}$ (for a given bedform aspect ratio). As a result,

$$\frac{H_f}{h_{\max}} \propto \rho^{-\frac{1}{6}} \propto p^{-\frac{1}{6}} \tag{7}$$

at a constant temperature. This prediction, which relies on β being independent of atmospheric density, is well matched by the data ($R^2 = 0.98$; Fig. 5b).

At Earth pressure, drag ripples cannot form and $\frac{H_f}{h_{\max}} \approx 90\%$. As pressure decreases, drag ripples form, protruding higher into the flow ($\frac{H_f}{h_{\max}} \approx 25\%$ at 500 mbar; Fig. 5b) enhancing the contribution of form drag to total aerodynamic roughness (Fig. 5a). As pressure further decreased in our experiments, the saltation layer thickened faster than drag ripples grew, such that $\frac{H_f}{h_{\max}}$ increased with decreasing pressure.

Whereas H_f increases with decreasing pressure, so does U_f, such that the behavior of $z_{0,\text{saltation}}$ may vary depending on specific
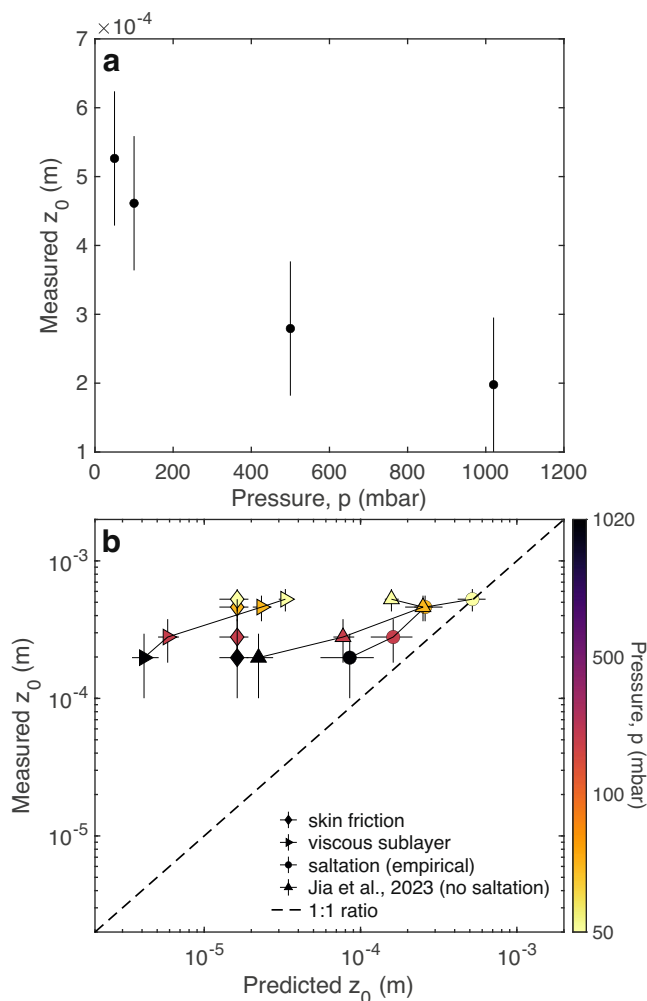
Fig. 4 | Aerodynamic roughness length. a Measured roughness length for different pressures. **b** Comparison of measured and modeled aerodynamic roughness length scales under Earth-to-Mars pressure conditions. Modeled values are estimated from the thickness of the viscous sublayer (Eq. (3)), skin friction (Eq. (4)), saltation-layer thickness (Eq. (6)), and compound roughness from skin friction and form drag from all bedform scales present[2] (Jia et al., 2023, no saltation). Source data are provided as a Source Data file.

transport conditions (Eq. (5)). In our experiments, wind speed was increased with decreasing pressure such that the freestream wind velocity remained about 20% above the saltation threshold (Methods). As a result, $z_{0,saltation}$ overall increased with decreasing pressure, enhancing the contribution of saltation to total aerodynamic roughness despite the formation of taller and taller drag ripples (Fig. 5). At 50 mbar, $\frac{H_f}{h_{max}} \approx 110\%$ and $\frac{z_{0,saltation}}{z_0} \approx 90\%$.

Implications for Mars

Our wind-tunnel experiments demonstrate that the roles of transport and bedforms on z_0 do not follow monotonic trends with atmospheric pressure, but instead are affected by interactions between bedform development and transport layer dynamics. Extrapolations to Mars-like conditions thus require careful considerations of these factors.

Dimensional analysis indicates that our experimental conditions capture the physical phenomenology expected on Mars (aerodynamically smooth beds conducive to drag-ripple formation with sand transport in saltation) for neutral atmospheric conditions (Supplementary Text S1 and Supplementary Table S1). Restated, experimental conditions reproduce the correct physical regimes despite different pressure conditions. The assumption of neutral atmospheric

conditions is implicit to Eq. 1. Theoretical[53], experimental[54], and in situ[44] evidence indicate that thermally induced variations in atmospheric conditions (e.g., from diurnal temperature swings) results in minor deviations in z_0 that are well within the uncertainty of our measurements (Supplementary Text S1 and Supplementary Table S1).

Based on our validation and calibration of Eqs. (8)–(9), we can estimate $z_{0,saltation}$ on Mars. In parallel, we estimate the combined contributions of skin friction and form drag from all bedform scales ($z_{0,bedforms}$) using the Jia et al. (2023) model[2] assuming grain and bedform sizes as measured at Gale crater (grain size, $d = 125\,\mu m$[55]; impact-ripple wavelength, $\lambda_i = 8$ cm; drag-ripple wavelength, $\lambda_l = 2$ m; bedform height-to-wavelength ratios of 0.05[36,42]). Typical values for Mars were used for all other parameters (e.g., $\rho = 0.020$ kg/m³, $\rho_s = 2900$ kg/m³, $g = 3.71$ m/s²). Both aerodynamic length scales are also compared with $z_{0,sublayer}$ (Eq. (3)).

We find that $z_{0,bedforms} \approx 1$ cm, which is consistently 1–2 orders of magnitude larger than $z_{0,sublayer}$ and $z_{0,saltation}$ across a range of plausible wind shear velocities (Fig. 6), i.e., it is 1–2 orders of magnitude larger than over a flat bed. Thus, z_0 is expected to be dominated by form drag over rippled beds on Mars regardless of whether transport is ongoing. This extrapolation implicitly relies on the assumption that flux saturation was reached within our wind-tunnel experiments. Estimates of the sediment transport saturation length under our experimental conditions are lower than the length of the wind-tunnel's test section (Methods), though the true distance required to reach saturation from a zero flux can be several times larger than the saturation length[56]. Measurements of impact-ripple migration speeds in the experiments ([40]; Supplementary Fig. S8) and our estimates of focal-height parameters (Supplementary Fig. S7) compare favorably with models that were developed to describe fully saturated conditions[22,49], suggesting that near-saturation conditions were likely reached. However, these models were themselves calibrated using empirical constants that could possibly obscure the signature of non-saturated transport conditions. If transport was substantially under-saturated in our experiments, the above extrapolations to Mars would underpredict $z_{0,saltation}$, rendering the contribution of saltation to z_0 comparable to that of form drag from bedforms.

Finally, we note that calculating r from $\max\left(z_{0,sublayer}, z_{0,saltation}\right)^2$, we find that $Re_r < 10$—even during active transport—over flat beds on Mars. Specifically, we find that wind shear velocities, $u_* > 1$ m/s are required for Re_r to exceed 10. Extrapolated to the height of the wind sensor onboard NASA's Curiosity rover (1.5 m above ground), such wind shear velocities correspond to wind speeds of >22.5 m/s (Eq. (1)), or stronger than over 99.9% of winds measured by Curiosity at Gale Crater[57]. This result is significant because it disproves the notion that saltation on Mars would inhibit the formation of drag ripples by promoting aerodynamically rough flat-bed conditions.

Methods
Experimental conditions
Experiments were conducted in the Mars Surface Wind Tunnel (MARS-WIT) at the Planetary Aeolian Laboratory, NASA Ames Research Center, California. The MARSWIT operates within a pressure chamber capable of simulating Earth-to-Mars pressure conditions (~1 bar–5 mbar). This 13-m long, open-circuit, atmospheric boundary layer wind tunnel can achieve maximum wind speeds of 100 m/s at 5 mbar using air injectors. LabView data acquisition software is utilized for operations, measuring, and providing data on chamber temperature, air density, pressure, freestream, and vertical differential pressures, pitot tube vertical position, relative humidity, and corresponding wind speeds. The pitot tube was placed at the downwind end of the test section. The test section was ~6.5 m long and 1.3 m wide (Fig. 1).

For each experiment, pressure, air density, and temperature were recorded, and the dynamic viscosity of air was assumed to be 1.81×10^{-5} Pa s. Crushed nutshells ($\rho_s = 1300$ kg/m³) served as sediment
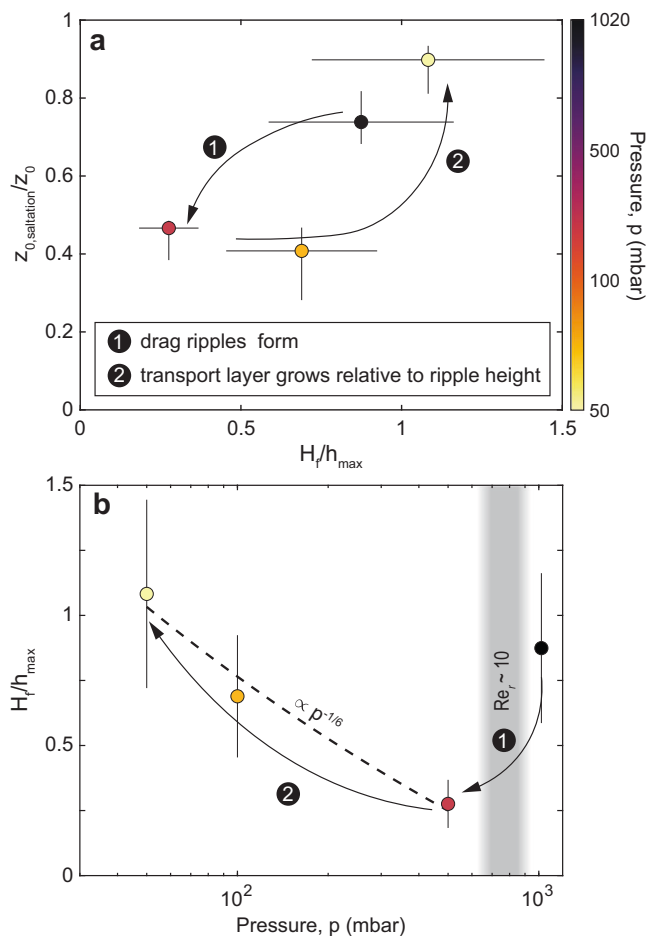
Fig. 5 | Influence of saltation on aerodynamic roughness under varied atmospheric pressures. a Ratio of aerodynamic roughness induced by saltation, $z_{0,saltation}$ (modeled) and z_0 (experimental measurements) as a function of the focal height, H_f, normalized by the height of the largest ripples present, h_{max}, at each pressure. **b** Ratio of focal height to maximum bedform height, H_f/h_{max}, as a function of pressure. Shaded area indicates the boundary between aerodynamically smooth and aerodynamically rough conditions (defined by Re_r ~ 10). Source data are provided as a Source Data file.
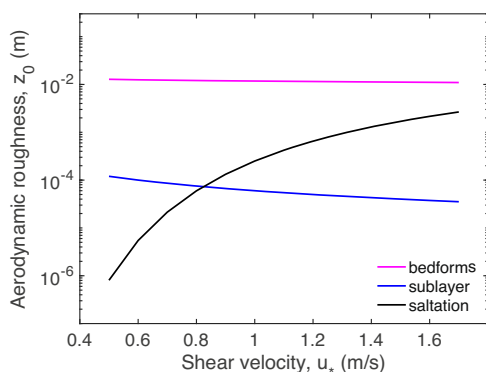
Fig. 6 | Aerodynamic roughness, z_0, as a function of shear velocity, u_*, on Mars. Aerodynamic roughness due to compounded skin friction and bedforms (bedforms) was calculated using the Jia et al. (2023) model[2]. Aerodynamic roughness due to saltation (saltation) was estimated using the Andreotti (2004) model[22] and Eq. (5), along with calibrated values of α and β (Eqs. (8)–(9)). Source data are provided as a Source Data file.

with a median particle size (d_{50}) of 195 μm. Grain-size distributions were determined using a Retsch Camsizer grain-size analyzer. Nutshells were used not to simulate Mars' lower gravitational acceleration ($g = 3.71$ m/s²) on saltation trajectories but to reduce the time required to generate bedforms under our lowest experimental pressure conditions (50 and 100 mbar)[40]. A manually smoothed, flat sediment bed was initially prepared inside the wind tunnel before each experiment, ensuring uniform sediment distribution across the test section (Supplementary Fig. S2). The bed had a thickness of 3 cm across the wind tunnel, and a sediment berm was placed at the upwind end of the bed to act as a continuous sediment source.

Two series of experiments were performed. In the first series, we determined the onset of saltation over flat beds by progressively increasing the wind speed until the bed became fully mobile[58]. This setup allowed for the determination of the threshold freestream (U_∞) and shear (u_{*t}) velocities over a flat bed at pressures of 50, 100, 500, and 1020 mbar (Supplementary Fig. S3). In the second series, the wind velocity was set ≈20% above the threshold freestream velocity, and maintained for several minutes to allow the sediment bed to evolve naturally from a flat to a rippled configuration. Once the ripples reached equilibrium, wind velocity measurements were performed at pressures of 50, 100, 500, and 1020 mbar. In the latter series of experiments, multiple runs (pumpdowns) were sometimes necessary at a given atmospheric pressure to replenish the berm and maintain depositional conditions while the bedforms reached equilibrium. For the 1020 mbar and 500 mbar experiments, a single pumpdown sufficed, while the 100 mbar experiments required two pumpdowns, and the 50 mbar experiments required three. Transport saturation lengths under our experimental conditions were estimated two different ways using the formulations in refs. 20,39, and were found to always be shorter to comparable to the length of the test section (~6.5 m), even under our lowest pressure condition (~5.5–6 m at 50 mbar).

Ripple dimensions
At each specific pressure, the evolution of the bedforms was continuously recorded with high-resolution infrared cameras at 30 fps, which provided top-down, side, and windward views of the test section (Fig. 1). This setup enabled precise measurement of the wavelength and migration rate (celerity) of incipient ripples and their final stabilized states. Each test concluded once the bedforms ceased growing, indicating equilibrium (Fig. 1c). At the end of each experiment, after the winds stopped, the pressure chamber was reset to ambient pressure. This allowed for additional documentation of the final bed state through three-dimensional (3D) scans and high-resolution color imaging. 3D scans were acquired using LiDAR sensors built into an iPad Pro 4th generation[59] with Pix4Dcatch software, and the data were processed with MeshLab 2023.12 (Supplementary Fig. S4). These scans allowed us to document the dimensions of equilibrium bedforms along downwind-oriented topographic profiles, including crest-to-crest wavelength and trough-to-peak height, under consistent lighting conditions. The 3D scans enabled the accurate calculation of the height and wavelength of drag (large) ripples, as well as the wavelength of the impact (small) ripples. The height of impact ripples was calculated as 5% of measured ripple wavelengths[60]. Calculated impact ripple heights range from ~1 to 3 mm at all pressures, in good agreement with ripple heights as determined from the length of ripple shadows at 50 mbar[40] (Supplementary Fig. S5). Bedform dimensions are reported in Supplementary Table S2 for each pressure condition.

Measurements of aerodynamic roughness length, z_0
Wind speed measurements were conducted using a pitot tube positioned at varying heights above the sediment bed. Wind velocity data were collected at four to five different vertical positions—at elevations of 4, 33, 103, 160, and 320 mm above the initial surface elevation—for

45–60 s at each position, with a sampling frequency of 0.3 Hz. The elevations were automatically set using a dedicated routine in Lab-View, with a precision of ±0.05 mm (Supplementary Fig. S1). The control system can maintain a constant wind speed with variations of less than 1% of the set value. In the same wind tunnel facility, ref. 58 performed wind measurements at nearly the same elevations above the bed to determine the threshold shear velocity of grains similar to those in this study. Changes in bed elevation were continuously monitored using a high-resolution infrared camera positioned for a side-view perspective. The initial height of the bed was checked relative to the position of the pitot tube and confirmed using a digital caliper. For experiments that required more than one pumpdown, i.e., at 100 and 50 mbar, the height of the bed was also monitored with a digital caliper between pumpdowns as the ripples started to form, and a new reference level was recorded.

The wind speed measurements were used to calculate the threshold shear velocity u_{*t} (flat-bed series) or shear velocity u_* (equilibrium-rippled bed) using the law of the wall (Eq. (1)). To that end, we used MATLAB's built-in Nonlinear Least Squares function. The method works by finding the parameters of a nonlinear model that minimize the sum of the squared differences (residuals) between the observed data and the model predictions (Eq. (1)). Instantaneous measurements provided sets of 135–180 data points for each elevation. The time between measurements at each elevation was 45–60 s, allowing to average wind measurements over turbulent fluctuations[3]. Only fits with R^2 values larger than 0.98 were considered, which resulted in the exclusion of 8–13% of the dataset. Remaining data were averaged to determine u_* and z_0 at each specific pressure (Fig. 3). As measurements for each elevation were repeated 2 or 3 times, an additional averaging process was performed to obtain the final values of u_* and z_0. Uncertainty in u_*, and u_{*t} was calculated as ± one standard deviation, and in z_0 as ± $d/2$. Values and uncertainties of u_{*t}, u_*, and z_0 for each pressure condition are reported in Supplementary Table S2.

Scaling relationship for the focal point

Ref. 22, using experimental surface roughness data from ref. 52, showed that under terrestrial conditions the focal velocity and focal height can be reasonably well predicted by

$$U_f \approx \alpha \sqrt{\frac{\rho_s}{\rho} g d}, \tag{8}$$

and

$$H_f \approx \beta_A U_f \left(\frac{\nu}{g^2}\right)^{1/3}, \tag{9}$$

where α and β_A are constants, ρ_s and ρ are the sediment and atmospheric densities, respectively, g is the acceleration of gravity, and d is grain diameter.

In turn, ref. 21 proposed a different formulation for the focal height,

$$H_f \approx \beta_{P+T} \left(\frac{\nu^2}{g}\right)^{1/3}, \tag{10}$$

where β_{P+T} is a constant.

Using an optimization subroutine, we minimized the difference between each of the two models and $z_{0,\text{saltation}}$. This approach allowed us to iteratively solve for sets of α and β parameters across all pressure conditions.

As reported in the main text, both models yield satisfying fits to the data, but β_{P+T} is not well approximated by a constant over the range of investigated pressures. Eqs. (8) and (9) were thus adopted, and the average of inverted α and β_A values were used in our analysis

(1.707 and 0.163, respectively; Fig. 2). Uncertainty in α and β was calculated as ± one standard deviation.

Model for aerodynamic roughness induced by multiscale topography

Experimentally derived z_0 values are compared to the theoretical model of ref. 2, which predicts the influence of multiscale topography (grains of size d, and small and large ripples characterized by wavelengths, λ, and amplitudes, ζ). In this model, z_0 is calculated for three scales by considering the roughness induced by grains on small ripples, the roughness induced by small ripples on large ripples, and the roughness induced by large ripples themselves. A complete description of the model can be found in ref. 2.

Our calculations of u_*, the height and wavelength of both small and large ripples ($h_{i,l}$ and $\lambda_{i,l}$), as well as the experimental data on kinematic viscosity of air, ν, and the median grain size ($d = 195 \, \mu m$), were used as input to the model. The effective roughness is calculated for a specific bedform aspect ratio,

$$k\zeta = \frac{2\pi}{\lambda_{i,l}} \frac{h_{i,l}}{2}, \tag{11}$$

where k is the bedform's wavenumber. Compound roughness values from skin friction and all bedform scales are reported for each pressure condition in Supplementary Table S2.

The model of ref. 2 underestimates measured z_0 values (Fig. 4) because, while it accounts for form drag from two scales of bedforms, it does not incorporate the influence of saltation. Thus, comparing measured and modeled values of z_0 allows to quantify the relative influence of saltation ($z_{0,\text{saltation}}$). The model of ref. 2 was used to that end as described in the Results and discussion section. To further validate this approach, the inverted value of $z_{0,\text{saltation}}$ at 1020 mbar was compared to predictions from numerical simulations[49] (Supplementary Fig. S6).

Data availability

The experimental parameters and derived measurements generated in this study are provided in the Supplementary Information file. Source data are provided with this paper.

Code availability

Code to reproduce the data shown in the figures is available in the Zenodo database under accession code https://doi.org/10.5281/zenodo.14970357.

References

1. Kok, J. F., Parteli, E. J., Michaels, T. I. & Karam, D. B. The physics of wind-blown sand and dust. *Rep. Prog. Phys.* **75**, 106901 (2012).
2. Jia, P., Andreotti, B. & Claudin, P. Hydrodynamic roughness induced by a multiscale topography. *J. Fluid Mech.* **974**, A16 (2023).
3. Stull, R. B. *An introduction to boundary layer meteorology* (Kluwer Academic Publishers, 1988).
4. Finnigan, J. Air flow over complex terrain. in *Flow and transport in the Natural Environment: Advances and Applications* 183–229 (Springer, 1988).
5. Raupach, M. Drag and drag partition on rough surfaces. *Bound. Layer Meteorol.* **60**, 375–395 (1992).
6. Kaimal, J. *Atmospheric Boundary Layer Flows: Their Structure and Measurement*, Vol. 289 (Oxford University Press, 1994).
7. Lancaster, N. & Baas, A. Influence of vegetation cover on sand transport by wind: field studies at Owens Lake, California. *Earth Surf. Process. Landf. J. Br. Geomorphol. Group* **23**, 69–82 (1998).
8. King, J., Nickling, W. & Gillies, J. Aeolian shear stress ratio measurements within mesquite-dominated landscapes of the Chihuahuan Desert, New Mexico, USA. *Geomorphology* **82**, 229–244 (2006).

9. Crago, R. D., Okello, W. & Jasinski, M. F. Equations for the drag force and aerodynamic roughness length of urban areas with random building heights. *Bound. Layer Meteorol.* **145**, 423–437 (2012).

10. Kent, C. W., Grimmond, S. & Gatey, D. Aerodynamic roughness parameters in cities: inclusion of vegetation. *J. Wind Eng. Ind. Aerodyn.* **169**, 168–176 (2017).

11. Courrech du Pont, S. et al. Complementary classifications of aeolian dunes based on morphology, dynamics, and fluid mechanics. *Earth Sci. Rev.* **255**, 104772 (2024).

12. García, M. H. Sedimentation Engineering. in *Sediment Transport and Morphodynamics* 21–163 (ASCE, 2008).

13. Nikuradse, J. Stromungsgesetze in rauhen rohren. *VDI forschungsh.* **361**, 1 (1933).

14. Yalin, M. S. *Mechanics of Sediment Transport* (Pergamon Press, 1972).

15. Einstein, H. A. *The bed-load function for sediment transportation in open channel flows* (US Department of Agriculture, 1950).

16. Meyer-Peter, E. & Müller, R. Formulas for bed-load transport. in *IAHSR 2nd meeting, Stockholm, Appendix 2* (IAHR, 1948).

17. Bagnold, R. A. *The Physics of Blown Sand and Desert Dunes* (Methuen, 1941).

18. Owen, P. R. Saltation of uniform grains in air. *J. Fluid Mech.* **20**, 225–242 (1964).

19. Farrel, E. & Sherman, D. Process-scaling issues for aeolian transport modeling in field and wind tunnel experiments: roughness length and mass flux distributions. *J. Coast. Res.* SI39, 384–389 (2006).

20. Durán, O., Andreotti, B., Claudin, P. & Winter, C. A unified model of ripples and dunes in water and planetary environments. *Nat. Geosci.* **12**, 345–350 (2019).

21. Pähtz, T. & Tholen, K. Aeolian sand transport: scaling of mean saltation length and height and implications for mass flux scaling. *Aeolian Res.* **52**, 100730 (2021).

22. Andreotti, B. A two-species model of aeolian sand transport. *J. Fluid Mech.* **510**, 47–70 (2004).

23. Durán, O. & Herrmann, H. Modelling of saturated sand flux. *J. Stat. Mech. Theory Exp.* **2006**, P07011 (2006).

24. Charnock, H. Wind stress on a water surface. *Q. J. R. Meteorol. Soc.* **81**, 639–640 (1955).

25. Sherman, D. J. An equilibrium relationship for shear velocity and apparent roughness lenght in aeolian saltation. *Geomorphology* **5**, 419–431 (1992).

26. Sherman, D. J. & Farrell, E. J. Aerodynamic roughness lengths over movable beds: comparison of wind tunnel and field data. *J. Geophys. Res.* **113**, F02S08 (2008).

27. Field, J. & Pelletier, J. Controls on the aerodynamic roughness length and the grain-size dependence of aeolian sediment transport. *Earth Surf. Process. Landf.* **43**, 2616–2626 (2018).

28. Basu, S., Richardson, M. I. & Wilson, R. J. Simulation of the martian dust cycle with the GFDL Mars GCM. *J. Geophys. Res.* **109**, E11006 (2004).

29. Kahre, M. A., Murphy, J. R. & Haberle, R. M. Modeling the martian dust cycle and surface dust reservoirs with the NASA Ames general circulation model. *J. Geophys. Res.* **111**, E06008 (2006).

30. Alvarez, C. A. et al. Direct measurements of dust settling velocity under low-density atmospheres using time-resolved particle image velocimetry. *Geophys. Res. Lett.* **51**, e2024GL109958 (2024).

31. Vermeesch, P. & Drake, N. Remotely sensed dune celerity and sand flux measurements of the world's fastest barchans (Bodélé, Chad). *Geophys. Res. Lett.* **35**, L24404 (2008).

32. Bridges, N. et al. Earth-like sand fluxes on Mars. *Nature* **485**, 339–342 (2012).

33. Arvidson, R., Guinness, E. & Lee, S. Differential aeolian redistribution rates on Mars. *Nature* **278**, 533–535 (1979).

34. Day, M. & Dorn, T. Wind in Jezero crater, Mars. *Geophys. Res. Lett.* **46**, 3099–3107 (2019).

35. Golombek, M. & Bridges, N. Erosion rates on mars and implications for climate change: constraints from the Pathfinder landing site. *J. Geophys. Res. Planets* **105**, 1841–1853 (2000).

36. Lapôtre, M. et al. Large wind ripples on Mars: a record of atmospheric evolution. *Science* **353**, 55–58 (2016).

37. Lapôtre, M., Ewing, R. C. & Lamb, M. P. An evolving understanding of enigmatic large ripples on Mars. *J. Geophys. Res. Planets* **126**, e2020JE006729 (2021).

38. Rubanenko, L., Lapôtre, M., Ewing, R. C., Fenton, L. K. & Gunn, A. A distinct ripple-formation regime on Mars revealed by the morphometrics of barchan dunes. *Nat. Commun.* **13**, 7156 (2022).

39. Yizhaq, H. et al. Coevolving aerodynamic and impact ripples on Earth. *Nat. Geosci.* **17**, 66–72 (2024).

40. Alvarez, C. A., Lapôtre, M. G., Swann, C. & Ewing, R. C. Ripples formed in low-pressure wind tunnels suggest Mars's large wind-blown ripples are not impact ripples. *Nat. Commun.* **16**, 2945 (2025).

41. Lapôtre, M., Lamb, M. P. & McElroy, B. What sets the size of current ripples? *Geology* **45**, 243–246 (2017).

42. Lapôtre, M. et al. Morphologic diversity of Martian ripples: implications for large-ripple formation. *Geophys. Res. Lett.* **45**, 10–229 (2018).

43. Van Rijn, L. C. Sediment transport, part III: bed forms and alluvial roughness. *J. Hydraul. Eng.* **110**, 1733–1754 (1984).

44. Sullivan, R. et al. Results of the Imager for Mars Pathfinder windsock experiment. *J. Geophys. Res. Planets* **105**, 24547–24562 (2000).

45. Andreotti, B., Claudin, P., Iversen, J. J., Merrison, J. P. & Rasmussen, K. R. A lower-than-expected saltation threshold at Martian pressure and below. *Proc. Natl. Acad. Sci. USA* **118**, e2012386118 (2021).

46. Vaz, D. A., Silvestro, S., Chojnacki, M. & Silva, D. C. Constraining the mechanisms of aeolian bedform formation on Mars through a global morphometric survey. *Earth Planet. Sci. Lett.* **614**, 118196 (2023).

47. Bagnold, R. A. The movement of desert sand. *Proc. R. Soc. Lond. Ser. A Math. Phys. Sci.* **157**, 594–620 (1936).

48. Ungar, J. E. & Haff, P. Steady state saltation in air. *Sedimentology* **34**, 289–299 (1987).

49. Durán, O., Claudin, P. & Andreotti, B. On aeolian transport: grain-scale interactions, dynamical mechanisms and scaling laws. *Aeolian Res.* **3**, 243–270 (2011).

50. Ho, T. D., Valance, A., Dupont, P. & El Moctar, A. O. Aeolian sand transport: length and height distributions of saltation trajectories. *Aeolian Res.* **12**, 65–74 (2014).

51. Valance, A., Rasmussen, K. R., El Moctar, A. O. & Dupont, P. The physics of aeolian sand transport. *C. R. Phys.* **16**, 105–117 (2015).

52. Rasmussen, K. R., Iversen, J. D. & Rautahemio, P. Saltation and wind-flow interaction in a variable slope wind tunnel. *Geomorphology* **17**, 19–28 (1996).

53. Monin, A. S. & Obukhov, A. Basic laws of turbulent mixing in the surface layer of the atmosphere. *Contrib. Geophys. Inst. Acad. Sci. USSR* **151**, e187 (1954).

54. White, B. R. Martian dust threshold measurements heated surface conditions. *Sand Dust Mars* **10074**, 58 (1991).

55. Weitz, C. M. et al. Sand grain sizes and shapes in eolian bedforms at Gale Crater, Mars. *Geophys. Res. Lett.* **45**, 9471–9479 (2018).

56. Selmani, H., Valance, A., Ould El Moctar, A., Dupont, P. & Zegadi, R. Aeolian sand transport in out-of-equilibrium regimes. *Geophys. Res. Lett.* **45**, 1838–1844 (2018).

57. Viúdez-Moreiras, D. et al. Gale surface wind characterization based on the Mars Science Laboratory REMS dataset. Part II: wind probability distributions. *Icarus* **319**, 645–656 (2019).

58. Swann, C., Sherman, D. & Ewing, R. Experimentally derived thresholds for windblown sand on Mars. *Geophys. Res. Lett.* **47**, e2019GL084484 (2020).

59. Luetzenburg, G., Kroon, A. & Bjørk, A. A. Evaluation of the apple iphone 12 Pro LiDAR for an application in Geosciences. *Sci. Rep.* **11**, 1–9 (2021).

60. Ellwood, J. M., Evans, P. D. & Wilson, I. G. Small-scale aeolian bedforms. *J. Sediment. Res.* **45**, 554–561 (1975).

Author contributions

C.A.A. and M.G.A.L. designed the experiments, and C.A.A. performed the experiments. C.A.A., M.G.A.L., C.S., R.C.E., P.J. and P.C. contributed to the conceptualization and formal analysis. C.A.A. and M.G.A.L. wrote the paper. P.J. ran the multi-scale topography model. All authors discussed the results and implications and commented on the paper at all stages.

Competing interests

The authors declare no competing interests.

Additional information

Supplementary information The online version contains supplementary material available at https://doi.org/10.1038/s41467-025-60212-7.

Correspondence and requests for materials should be addressed to Carlos A. Alvarez.

Peer review information *Nature Communications* thanks Thomas Pähtz and the other anonymous reviewers for their contribution to the peer review of this work. A peer review file is available.

Reprints and permissions information is available at http://www.nature.com/reprints

Publisher's note Springer Nature remains neutral with regard to jurisdictional claims in published maps and institutional affiliations.